# A new paradigm for numerical simulation of microneedle based drug delivery aided by histology of microneedle pierced skin

**Tao Han, Diganta Bhusan Das***

Chemical Engineering Department, Loughborough University, Loughborough LE11 3TU, Leicestershire, UK

(*Corresponding author; Email: D.B.Das@lboro.ac.uk)

**Abstract**

Microneedle (MN) is a relatively recent invention and an efficient technology for transdermal drug delivery (TDD). Conventionally, the mathematical models of MNs drug delivery define the shape of the holes created by the MNs in the skin as the same as their actual geometry. Furthermore, the size of the MN holes in the skin is considered to be either the same or a certain fraction of the lengths of the MNs. However, the histological images of the MN treated skin indicate that the real insertion depth is much shorter than the length of the MNs and the shapes may vary significantly from one case to another. In addressing these points, we propose a new approach for modelling MN based drug delivery, which incorporate the histology of MN pierced skin using a number of concepts borrowed from image processing tools. It is expected that the developed approach will provide better accuracy of the drug diffusion profile. A new computer program is developed to automatically obtain the outline of the MNs treated holes and import these images into computer software for simulation of drug diffusion from MN systems. This method can provide a simple and fast way to test the quality of MNs design and modelling, as well as simulate experimental studies, e.g., permeation experiments on MN pierced skin using diffusion cell. The developed methodology is demonstrated using two dimensional (2D) numerical modelling of flat MNs (2D). However, the methodology is general and can be implemented for 3D MNs if there is sufficient number of images for reconstructing a 3D image for numerical simulation. Numerical modelling for 3D geometry is demonstrated by using images of an ideal 3D MN. The methodology is not demonstrated for real 3D MN as there are not sufficient numbers of images for the purpose of this paper.

**Keywords:** Transdermal drug delivery, microneedles, numerical modelling and simulation, histological image, diffusion, Canny edge detection

## 1. Introduction

Transdermal drug delivery (TDD) methods, which intend to deliver various drugs through the skin, need to conquer the outermost layer of the skin, namely, the *stratum corneum* (SC) [1]. Mathematical modelling of drug transport through the skin can provide important insights into TDD and it is considered to be important for analysing TDD as indicated by a large number of studies [2, 3]. This paper aims to report a new paradigm for numerical simulation of microneedle (MN) based drug delivery aided by histology of the MN treated skin.

The importance of the physicochemical properties of solutes for transdermal permeation has been known since the early 1940s. But, it is only since the 1960s, i.e., when Higuchi first related these properties to passive diffusion in percutaneous absorption of drug molecules [4] using Fick's first law of diffusion that modelling diffusion of drugs for TDD has been seriously attempted. Based on the diffusion law, many researchers have now simulated drug transport from different technologies that can enhance the TDD [5]. MN technology is a promising method and it is increasingly being explored for controlled enhancement of TDD of different molecules [6, 7].

The first MN modelling paper aimed to aid design of hollow MNs for fluid extraction [8]. Since then, various researchers have focussed on improving the accuracy of simulation by incorporating important fundamental features of the behaviour of MNs for drug delivery, thereby, achieving better prediction of the drug diffusion behaviour [9, 10]. For example, the geometry and size of the MNs, which are important factors, have been considered in a number of previous modelling studies because they determine the drug diffusion rate and flux from the MNs [11]. Consequently, optimization of the MNs geometry, shape and size of the MNs has been attempted by many researchers, so that the desired TDD rate can be identified for specific case [12]. These frameworks demonstrate that the patterns of MNs and alignment of these MNs on the patch are important to provide a sufficient delivery rate of drugs [13].

Overall, it seems that the simulations for MNs based drug delivery are helpful for design of MNs and understanding how they function but these require results of high quality and accuracy. Generally, the current researches on MNs modelling idealize the size and shapes of the MN holes (i.e., the computational domain) which are created by the MNs and often it is assumed that the size of the holes are the same as the MNs themselves or a certain fraction of the lengths of the MNs. However, the histological images of these holes indicate that the shapes of MNs and their associated holes may be very different [14]. Not only the lengths of the MNs pierced holes vary in length from case to case but also their shapes may vary. From the point of view of TDD, this implies that the drug delivery rate should vary from case to case. This can become a crucial factor that causes inaccuracy in the simulation results. For these reasons, this

paper aims to develop a new paradigm in numerical simulation for drug delivery by MNs which can incorporate the shapes and sizes of the MNs holes as determined from the histological images of MNs treated skin. It is hypothesised that more realistic simulated drug transport behaviour (e.g., transient drug concentration profile) can be obtained by averaging simulation results from a number cases given by different histological images for the same circumstance (e.g., the same skin, MN length and drug molecule), coupled with experimental data (e.g., diffusion coefficient of the drug or drug permeability) for the corresponding case.

In addressing this issue, this paper introduces a new approach that should improve the simulation accuracy of MNs based drug delivery. We present a numerical model based on the histological images of MNs treated skin instead of using the conventional method [15] which considers the geometry of MNs in conjunction with a correction factor to determine the lengths of the holes. There are several advantages of using these images, as discussed below.

When we consider the histological images and couple them with experimentally determined parameters (e.g., drug diffusion coefficient) for modelling the drug transport, the deformation of the skin due to insertion of MN [9, 16], which affects the drug transport behaviour, will be directly accounted for. Most MN drug delivery simulations tend to ignore the effects of skin deformation as it is governed by the geometry of the MNs, force exerted on the MN patch and viscoelastic properties of the skin, thereby, making skin deformation and its effect on drug transport a difficult quantify to determine. However, there are several researches which focused on studying the factors that can cause skin deformation, e.g., the MN insertion force has been decomposed into several components to increase the accuracy of the simulation [16]. Similarly, the viscoelastic properties of the skin layers have been considered [17]. The histological images provide a view of the holes created by MNs on skins. For the same cases, experimental data on drug permeation and effective diffusion coefficient can be obtained. The accuracy of the information can also be increased by acquiring a number of these images and experimental data. As stated earlier, it is hypothesised in this paper that these information can then be used to carry out more accurate numerical simulations for MN based drug delivery.

The histological image can provide an efficient way to evaluate the practicability of the MNs modelling and, the images may be acquired irrespective of the source or the method of acquiring them. For example, the cross-sectional view of the MNs treated skin can be acquired by using a cryotome and then viewed under a microscope [18]. Similarly, technologies such as optical coherence tomography (OCT) [19, 20] and micro-CT [21] have been useful in obtaining images of MN pierced skin. These images can show whether the pathways (holes) created by the MNs are adequate in overcoming the SC and for a target drug molecules to pass through.

In order to analyse the drug transport behaviour based on the histological images, a MATLAB program has been developed in this work which can automatically acquire the coordinates of various points of the image of the skin sample. These coordinates (i.e., not the image) can then be imported into a simulator (e.g., commercially available software COMSOL [22]) to carry out the desired simulations for drug transport.

## 2. Histology of MNs treated skin as computational domain for numerical simulation

### 2.1 Acquisition of images of MNs pierced skin

In this work, the computational domain for the numerical simulation is based on the histological images which can expose the cross-sectional views of MNs treated skin. The images are collected using porcine ear skin purchased from local abattoir [23]; however, the developed methodology is general and it would work with images collected via any other means.

The skin samples are freshly harvested and flash frozen using liquid nitrogen after sectioning and kept in the freezer at -20ºC if they are not used immediately after collection. The sample are wrapped in aluminium foil and left in room temperature to defrost for 2 hr before an experiment. The skin are cautiously separated from the underneath cartilage using a surgical scalpel.

1100µm/1400µm long MN patches which are purchased from nanoBioSciences (Sunnyvale, CA, USA) are used to pierce the skin. The insertion depths of these commercial MNs patches (~ 400 – 500 µm) are much shorter than the actual lengths of the MN as the insertion depths depend not only the actual MN lengths but also the force of insertion, MN density of the patches and viscoelasticity of the skin. These have been demonstrated in our previous paper [24] and are not discussed here.

A MNs patch is pushed with a relatively high thumb pressure to ensure that all the needles are pierced into the skin and then mounted to a pneumatic pump with a constant 1MPa pressure for 10min. The sectioning protocol for the prepared skin sample using cryotome (Fig. 1) is consistent with our previous study and is not discussed in detail in this paper [25]. The sample of sliced skin is then analysed under a microscope and a number of images are taken using a camera which is attached to the microscope. The acquired images are processed for numerical simulation as discussed below.

## 2.2 Processing of skin histological images for numerical simulations

An image of the skin histology cannot be directly used as a computational domain for numerical simulations as the skin layers/surfaces needs to be identified in terms of co-ordinate points. Furthermore, due to the possibility of a number of other factors which affect the quality of the original image for simulation purpose, the developed algorithm is designed to eliminate these factors. These are discussed separately in the latter part of the paper.

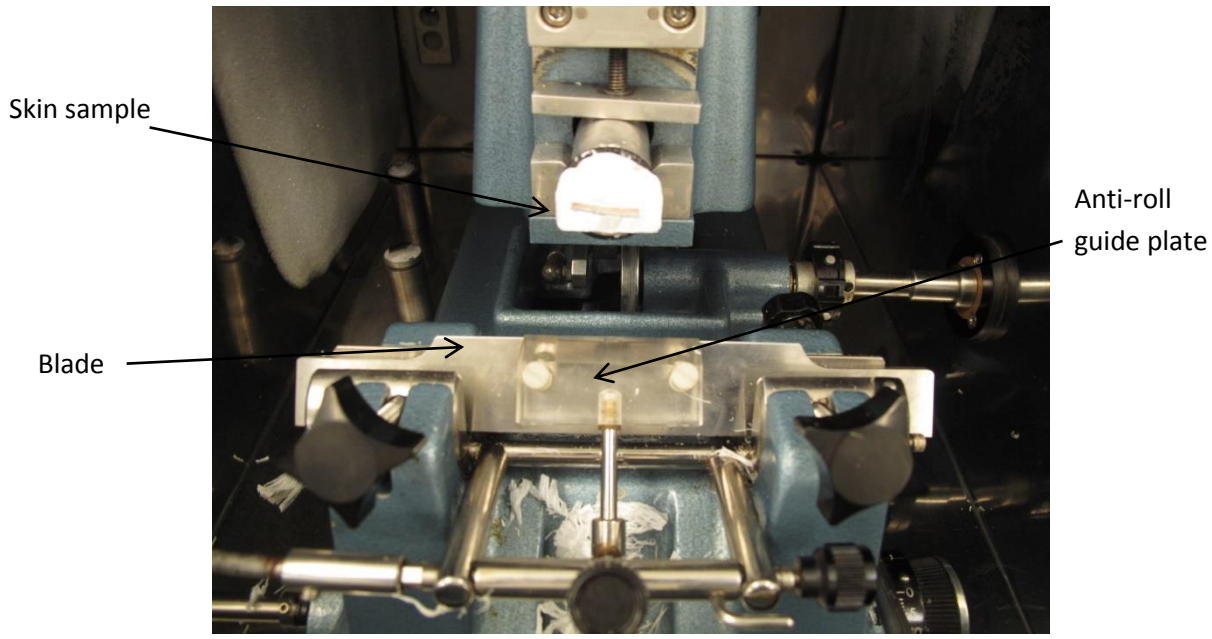


Fig. 1 A cryotome setup which was used to acquire the histological images of the MN pierced skin. The skin sample is wrapped in glue, fixed on the sample holder between the blade and anti-roll guide plate, and sliced into think sections.

Once the images of the cross-sectional view of the MN pierced skin samples are captured, all the images are imported into MATLAB (Natick, MA, USA) for processing [26]. In this work, an in-house MATLAB program was developed to process these images. The first step of this program is to acquire all the edges of the image. To achieve this, all RGB images (conventional format using red, green and blue added on each other to reproduce all colours) need to be converted into grayscale images. A Canny edge detection algorithm [27] is then applied on the grayscale images to acquire the edges of the individual images. A Canny algorithm is an advanced image filter based on a Gaussian filter [28]. It involves four stages, namely, (i) noise reduction, (ii) edge detection, (iii) edge thinning, and (iv) thresholding with any hysteresis, which provide high quality edges of computational domain in a black and white map. Two examples of images of skin pre-treated with MN, which have been processed with the Canny algorithm using the developed MATLAB code, are shown in Fig. 2. From the figure we can see that the edges of the original images are acquired with high quality details. However, in reality, we do not need all

the details in different skin layers as well as the debris outside the skin which do not have any significance for the drug transport. Furthermore, the presence of debris may influence the numerically determined transport behaviour. Therefore, the images obtained are further processed by specific algorithms to acquire smoother profiles of the skin layers/surfaces.

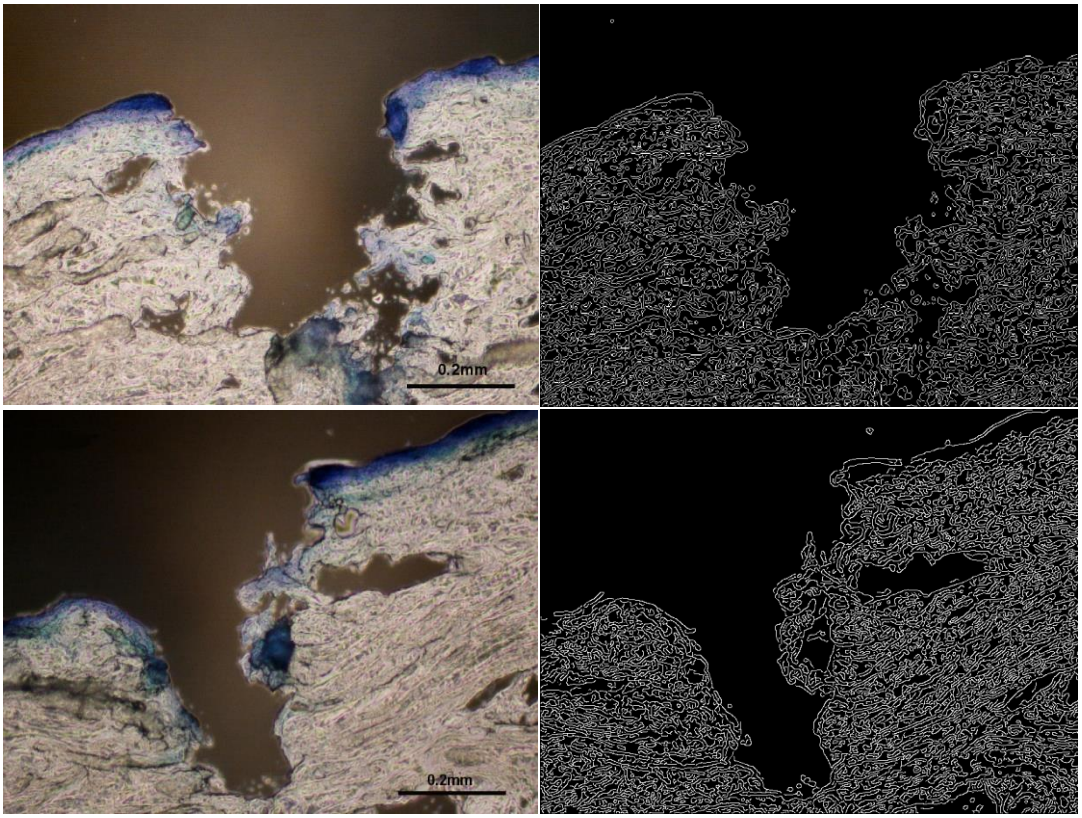


Fig. 2 Two examples of histological images of skin pierced with MNs (images on the right) which are treated with the Canny edge detection algorithm (images on the left) for further processing and numerical simulations.

### 2.2.1 Different steps adopted for smoothing the images of skin histology for numerical simulation

The algorithm for preparing the geometry of the computational domain for numerical simulation is consisted of four stages: (i) the image dilation and fill, (ii) debris identification, (iii) debris elimination and (iv) importing domain as computational domain for numerical simulation. When all four stages are finished, the acquired geometry of the domain is expected to be ready as a computational geometry for numerical simulations.

#### 2.2.1.1 Dilation and filling

Firstly, the edges acquired from the edge detection process need to be dilated to connect any gaps on the skin surfaces. It is a necessary step to accomplish an intact domain for numerical simulation from discrete lines as shown in Fig. 2 [29]. From a number of trials we have

concluded that a 5 pixels×5 pixels dilation matrix is sufficient to connect all the gaps in the images that we have collected. However, this matrix may be different in another case where the image of the skin histology is significantly more complicated and requires significant amount of dilation and filling. To achieve higher accuracy, the size of the matrix, represented as 'se' in this paper, can be modified in the developed program. After all the gaps have been connected, there may be still some undesired sections (e.g., holes or unconnected parts) left in the image, which need to be filled, as otherwise they would impede the process of the skin layer acquisition and numerical simulations. The boundary of the domain also needs to be defined according to the profile of skin surface before the 'image fill' process.

#### 2.2.1.2 Debris identification

As discussed above, after the computational domain (an image) has been confirmed, there may still be some undesired skin debris in it. The debris can be hard to predict in the images because they can be constituted by loose debris of the skin sample (e.g., generated while the skin is pierced) as well as by other impurities or bubbles in the embedding compounds (e.g., gels used for acquiring cryotome images). The MATLAB program has been developed to automatically identify all kinds of debris so as to smooth the images irrespective of their sources.

For the purpose of debris identification, the debris in the image is discriminated from the main body of the skin sample and the debris is identified individually by the program. After the debris is identified, an elimination program is launched to remove the debris. This stage of the developed program is designed to remove debris from the image without causing any damage to the computational domain of interest. Our method shows great advantages comparing to other filtration methods (such as using rank or Gaussian filtering methods to remove debris) whichcan cause great damage to the outline of the skin [30]. Fuller details of the debris elimination program will be introduced in section 2.2.1.3.

##### 2.2.1.2.1 Specifying corners of the debris in terms of co-ordinates

The debris identification stage is based on the assumption that the debris has closed edges/boundaries. In other words, if a point on the edge of debris moves along its edge, it will eventually come back to the same point where it started. This is an important factor in the developed algorithm so as to discriminate the debris from the skin sample and confirm which of the target debris is to be eliminated. If we choose a corner of the debris as the starting point, this point will then go from corner to corner and finally reach the original corner. Therefore, we need to classify the moving patterns between the corners. To explain this process a logic diagram is shown in the Fig. 3. In the figure, the capital letters L/R/U/D/T/B/P/N represent the initial alphabets of words left/right/up/down/top/bottom/positive/negative, respectively, which represent how a position moves in the algorithm to identify the debris. For example, the

combination of LTP indicates the following: (1) the current point is on one of the left (L) top (T) corners of the image; (2) the points on its lower right havetheir pixel intensity values equal to posititive (P) 1.0; and (3) positive represents the direction of the edge detecting process passing this point is clockwise (while negative represents counter-clockwise). In contrast, the LTN points satisfy the inverse of the above three conditions for LTP points. A schematic diagram to explain the differences between the LTP and LTN points has been shown in Fig. 4.

**2.2.1.2.2 Principles for the identification of debris**

In this section, we discuss the principles and the mechanism of the debris identification process in more detail. The developed MATLAB program starts from LTP which could be a positive left top corner of a domain of any shape. To define a corner in an image, we define that a minimum number of four points are required. In this specific case at point (x,y), a LTP can be confirmed if it satisfies the following four conditions: (x+1,y-1)=0; (x,y-1)=0; (x-1,y-1)=0 and (x-1,y)=0 (for a 800x600 image, the coordinate from left top to left bottom is x=0 to x=600, from left top to right top is y=0 to y=800). Once a LTP point is chosen, there are two initial conditions that should be satisfied for this program. Firstly, LTP is chosen as the only criterion being both the starting point and terminal point, and secondly, it is defined that the first move from LTP is always to the right direction (clockwise). From Fig. 3 we can see that there are only two destinations if a LTP point moves to the right following the edges, i.e., RTP and RBN. If a point reaches the RTP, then it can only move downward to either RBP or LBN. An example edge detection process has been shown in Fig. 5.

Although there are 8 different corners involved according to Fig. 3, they are all connected to the four terminals which are marked with different colours. They are LTP/RTN/LBN/RBP marked with red/purple/blue/green, respectively. However, only the red LTP is the real terminal. . When the process reaches red LTP, a check must be made to compare the current point to the original one. If they are the same point, it indicates that the edge detection process has been done because the selected point has travelled the entire surface of the debris and back to its original position again. If not, the process will go back to LTP① and continues until it reaches the original point. The circle enclosed number represents pathway 1 which is connecting LTP to either corner RTP or RBN. These pathways can keep the edge detection process to stay on the edge. Otherwise, the process may never move from one corner to another.

When the edge detection process reaches other three terminals, it will jump back to the previous junction that has the same colour with that terminal, for example, all purple RTN terminals will jump back to junction purple RTN⑥. An illustration of a simple loop starting from junction RTN⑥, which moves to terminal RTN following the edge of the shape and then jumps

back to junction RTN⑥, has been shown in Fig. 6. Where the blue and black arrows represent the process conducted in logic diagram and reality, respectively. When the process jumps back to the junction RTN⑥, the point will move to the left again until it reaches the terminal LTP. All three coloured junctions connect to a LTP terminal to avoid falling into infinite loops.

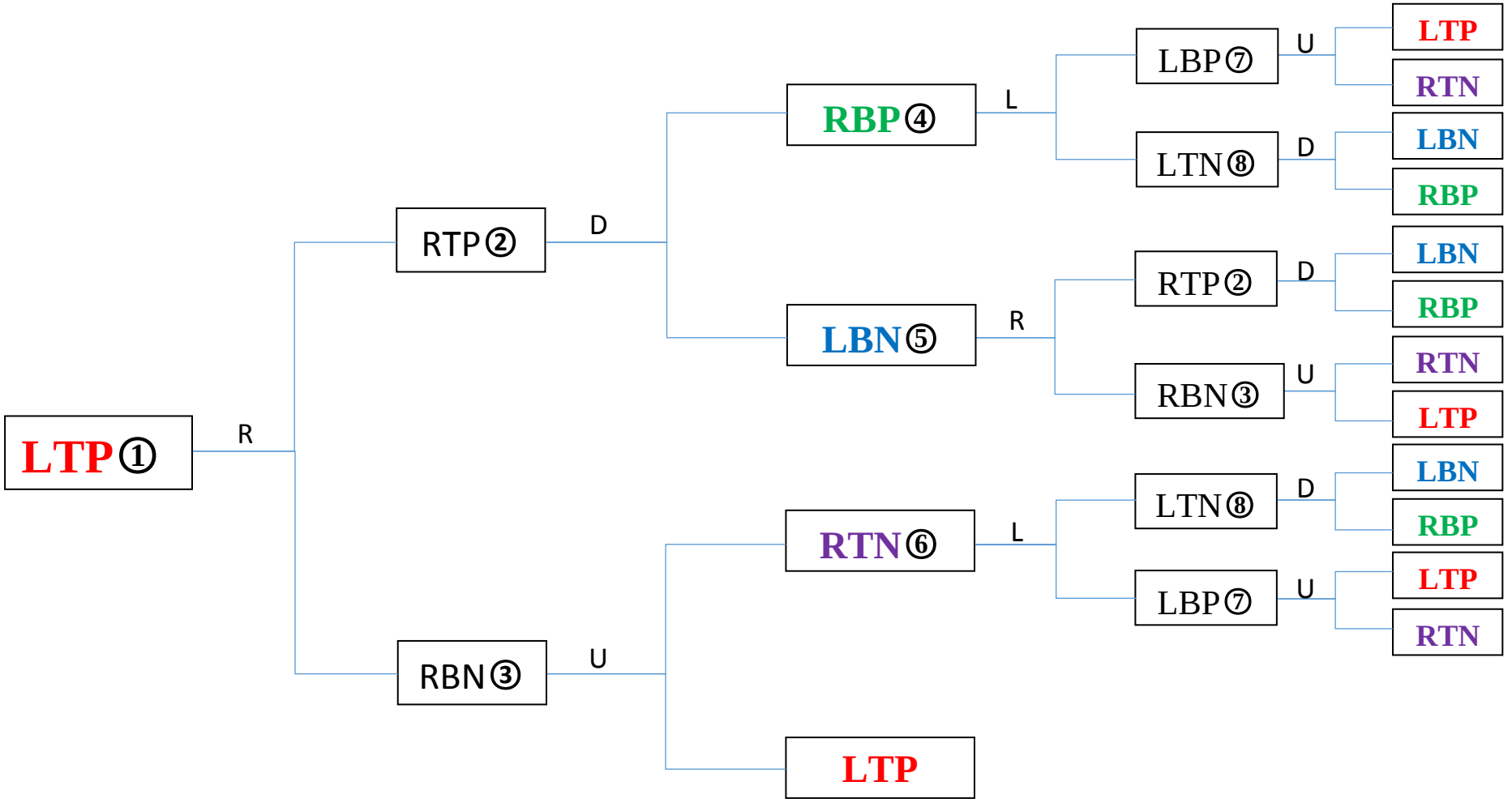


Fig. 3 A logic diagram of edge detection algorithm: L=left, R=right, U=up, D= down, T=top, B= bottom, P=positive, N=negative. Circle enclosed number represents pathways connected to specific corners.

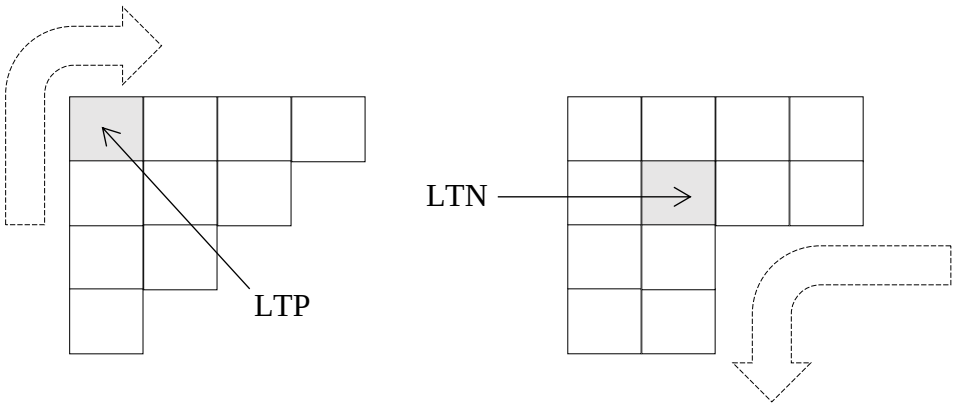


Fig. 4 A schematic diagram to demonstrate the differences between a LTP point and a LTN point (each square in the diagram represents one pixel in the image).

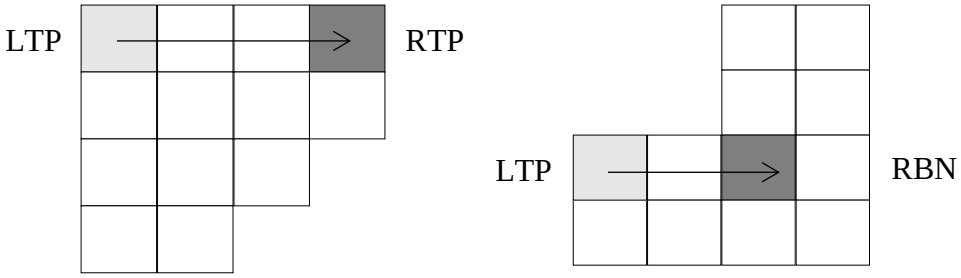


Fig. 5 A schematic diagram which shows two possibilities for a point while moving from LTP to either RTP or RBN (each square in the diagram represents one pixel in the image).

**2.2.1.2.3 The definition of hidden corners**

In some cases, there are corners which are not easy to distinguish from the shape because the definition of a corner in this program and it may not be possible to assign co-ordinates precisely to each point. This is because these corners are concealed in the shape or overlapped with other points. However, they can be found by the edge detection process. The reason for the existence of these hidden corners is that the trajectory of the edge detection process is not always straight. When the trajectory is terraced, the corner will appear as irregular. An illustration of hidden corners RBN and RTN in edge detection process has shown in Fig. 7.

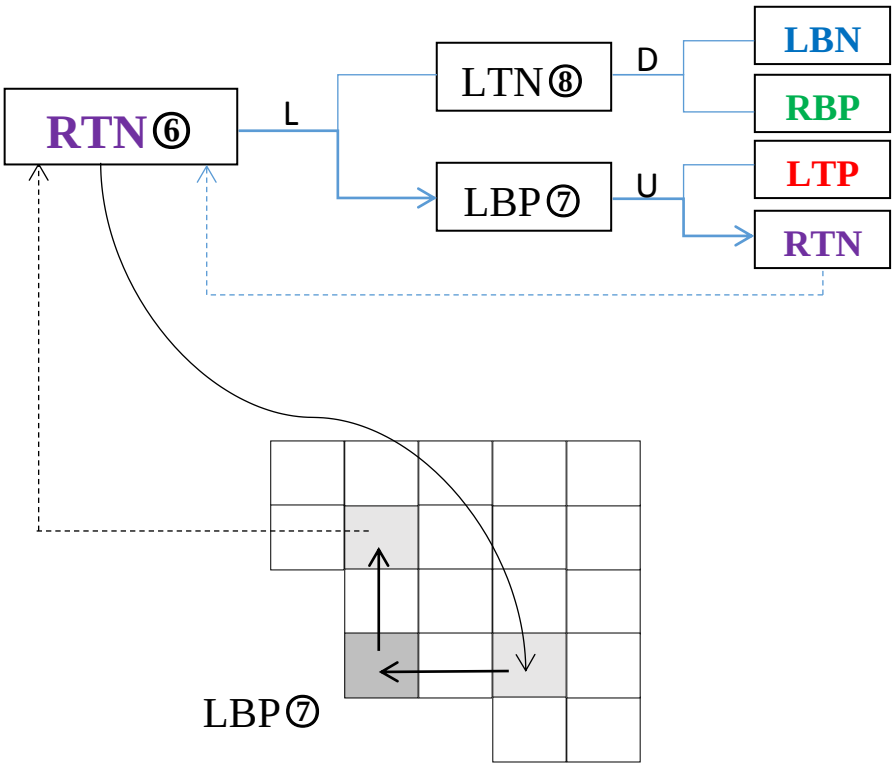


Fig. 6 An example of a typical case in which the debris identification process reaches a terminal (see Fig. 3) where it will automatically jump back to its corresponding junction (each square in the diagram represents one pixel in the image).

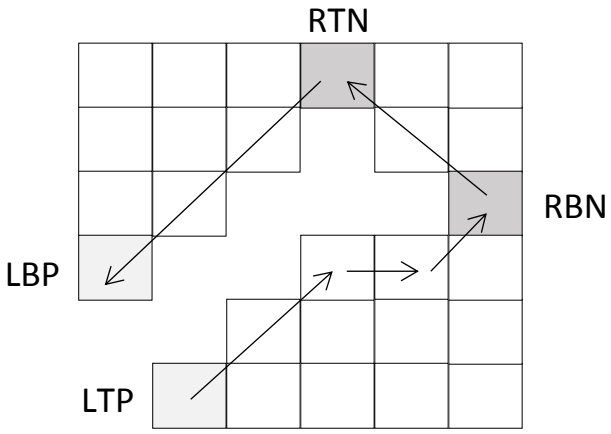


Fig. 7 Illustration of two hidden corners existing in this example figure, which are RTN and RBN formed due to terraced edge (each square in the diagram represents one pixel in the image).

The corners LTP and LBP are easy to identify but the corners of RBN and RTN are likely to be anomalous. Nevertheless, the RBN and RTN can be recognized by the program, and therefore, the developed MATLAB code will ensure that the edge detection process will not be affected.

#### 2.2.1.2.4 Special cases in the process of identifying corners

A special circumstance needs to be clarified when the edge detection process runs back to LTP from the only two possible corners: LBP and RBN. Three representative cases have been shown in Fig. 8:

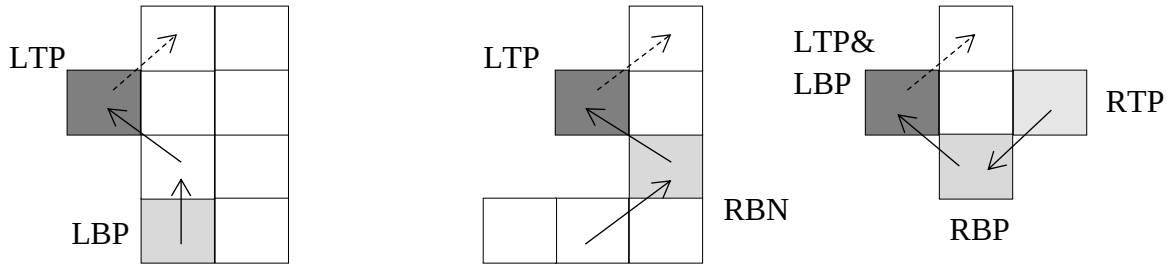


Fig. 8 Three special cases in the edge detection process which need to be identified individually in the program by the user (each square in the diagram represents one pixel in the image).

The first and second cases in Fig. 8 show that when the edge detection process moves up from LBP and RBN to LTP corner, the program will not be able to recognize the LTP corner according to the logic diagram. The program will ignore the LTP corner and move on to follow the dashed arrow. The third case shows an extreme circumstance in which the LTP corner overlaps the LBP corner and the program will go on following the dashed arrow. The reason for this situation is due to the fact that when we define the LTP corner, we have used four points. However, only three points have been used to profile the pathways. The problem for all other corners has been solved by applying the 'hidden corner' concept which has been mentioned previously. But the LTP corner is different because the program may have to be terminated here. To solve this special case, an additional step must be introduced to compare the current LTP corner to the original one. Once the left top corner is confirmed as the same one of the original corner, it indicates that one of the debris has been identified so that the corresponding elimination process will be triggered.

#### 2.2.1.3 Debris elimination

Once all the debris has been identified, the program will jump to the elimination stage automatically to remove the skin debris. As mentioned before, a conventional image filter cannot be applied here due to the inaccuracy [31]. Therefore, the elimination process is specially designed which shares the same logical diagram with the debris identification process. However, the elimination process will erase every point that the moving point Y has passed through. Therefore, the program will not stop until the last point of the debris is eliminated because the starting point has already been erased at the beginning. The elimination program peels off the debris shape layer by layer and jumps back to the debris identification program once the process is finished. An illustration of the elimination process is shown in Fig. 9.

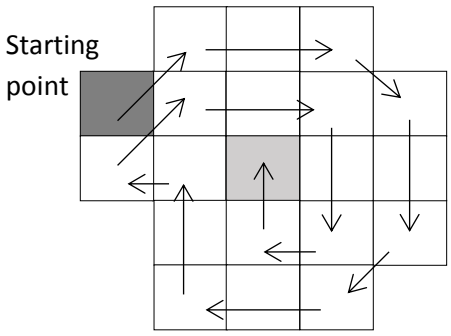


Fig. 9 An illustration of the debris elimination process (each square in the diagram represents one pixel in the image).

The elimination process begins from the starting point which is a LTP corner of the shape and will be at the middle point of the shape that marked in light grey colour. However, the elimination process may not be able to finish in one go because sometimes the shape will be broken into several small blocks. It happens when the connection point is erased so that the moving point Y cannot go back to the original block to finish the elimination process. To solve this problem, the identification process is always scanning line by line from top to bottom. Once the first starting point is identified, the program will jump to elimination process to remove the debris. After the elimination, the identification program will scan the next line and find the second starting point to remove the remaining part of the debris. The illustration is shown in Fig. 10.

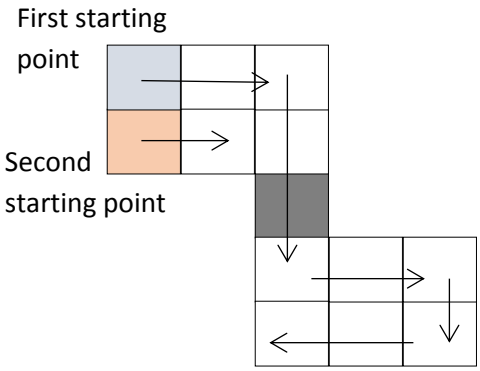


Fig. 10 An illustration for the special elimination case, first starting point, second starting point and the connection points are marked with light blue, pink and grey, respectively (each square in the diagram represents one pixel in the image).

To increase the speed of the program, a global parameter ‘si’ is set to describe the maximum size of debris. The ‘si’ parameter is pre-set to 30 in this work, which means that the maximum size of debris in an image is equal to or smaller than 30x30 pixels. After all debris are identified and eliminated, the program will move to the next stage and the treated image compared to the untreated image is shown in Fig. 11.

## 3 Numerical simulations using processed image

### 3.1 Acquiring processed image in numerical simulator

After the debris identification and elimination process, the image shows clear outline of the skin sample without the interference of the debris. The program then captures the profile of the skin by picking up all the points on the boundary. The thickness of the profile is defined to be one pixel and the acquired profile will be saved in a matrix.

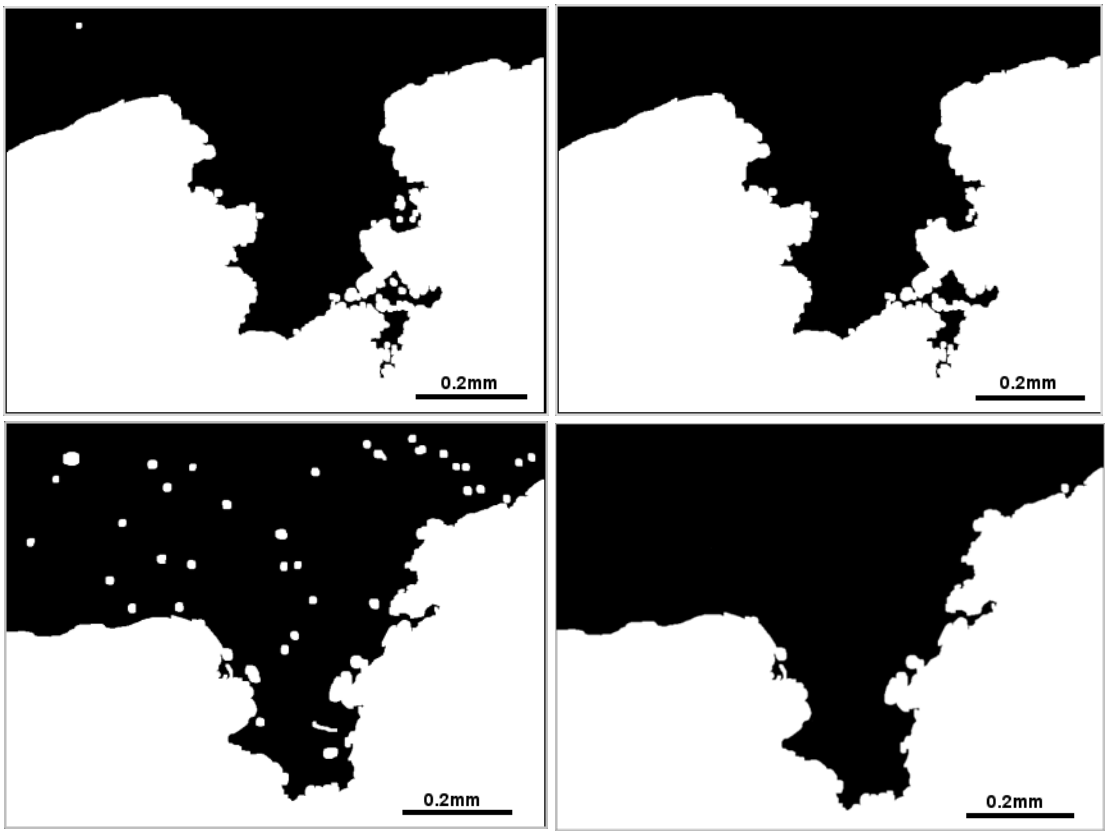


Fig.11 Two pairs of typical images before (left) and after (right) treating with debris identification and elimination stages. The two images on the right hand (top and bottom images) side are now ready to be used as computational domains for numerical simulation.

To carry out the diffusion analysis, the profile of the skin is imported into a commercially available FEM software (COMSOL) in this work. However, it can be imported to any numerical software or environment. All the coordinates of the points that are required for geometry are saved in a [n,2] matrix and the order of the coordinate of points are also properly reorganized. To achieve the same geometry between the computational domain in the FEM software and the imported domain, the rearranged coordinate in the matrix must represent adjacent points in the image.

After the profile of the skin surface has been acquired, the computational domain is converted into computational geometry whose boundary is consisted by coordinate of points (instead of

boundary lines as seen in an image). This imported geometry is then meshed for numerical simulation. An example of a numerical mesh is shown in Fig. 12. The coordinates of all points in the mesh are saved in a .txt file by the program, so the simulation can be done using any software. There is only one task that needs to be done by the users themselves, which is to find the ratio between the pixel and scale of the actual image. This requires user to set up a scale when they obtain an image using camera, micro-scope, OCT or micro-CT or any other source. After the scale is known, the ratio can be easily calculated by an image processing software.

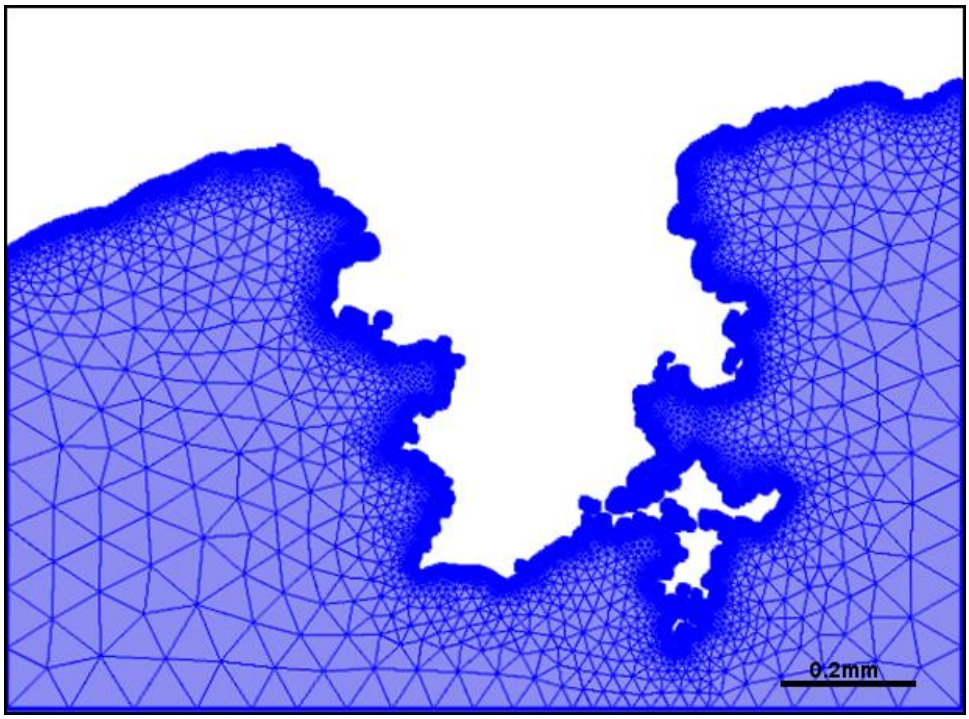


Fig. 12 A typical image of a histological image which is meshed for numerical simulation

### 3.2 Governing equations

As discussed earlier in our papers, an effective skin thickness can be defined for MN treated skin which represents the average path length for drug diffusion through the skin [32, 33]. Using the same concept, we calculate the effective thickness in this work using the images that we have collected. We define that there is negligible change on the diffusion coefficient in viable epidermis due to insertion of MNs and the diffusion profile of drug molecules passing through the skin at steady state is obtained using the Fick's first law:

$$\boldsymbol{N_i = -D_i \nabla C_i} \quad (1)$$

Where $\mathbf{N}_i$ is the flux, the $\mathbf{D}_i$ is diffusion coefficient, $\mathbf{C}_i$ is the concentration. In the simulation of MNs treated skin and the thickness of the skin change, so the effective thickness of the skin is introduced in consistent with our previous studies [32, 33]. Therefore, we deduce the diffusion coefficient from the experiment data of passive diffusion and the effective thickness in this study

can be simply considered as reduction of the real skin thickness. The real skin thickness is 1.6 mm which is the average over 20 randomly selected samples. An effective thickness of the MNs treated skin is then calculated using equations (2) and (3) as discussed earlier [33].

$$\boldsymbol{D_{PD}} = \frac{\boldsymbol{J_{PD}h}}{\boldsymbol{\Delta C}} \tag{2}$$

$$\boldsymbol{h_{eff}} = \frac{\boldsymbol{D_{PD}\Delta C}}{\boldsymbol{J_{MN}}} \tag{3}$$

Where $J_{PD}$ is the flux from passive diffusion, $J_{MN}$ is the flux from MNs treated diffusion, $D_{PD}$ is the diffusion coefficient of the skin and $h_{eff}$ is the effective thickness of the MNs treated skin. We use the steady state model to analyse the experimental data because it is impossible to know the drug concentration at any position of the skin at any time point. However, the numerical simulation is able to provide simulated data at any specific time point and depth [34].

Once the effective skin thickness has been identified, we apply Fick's second law in order to build a transient drug diffusion model:

$$\frac{\partial c_i}{\partial t} + \nabla \cdot (-D_i \nabla c_i) = R_i \tag{4}$$

Where $\mathbf{c}_i$ is the drug concentration, D is the diffusion coefficient, t is the time point and $R_i$ is a constant.

The 1D boundary conditions to solve the differential equations (1) and (4) are:

$$\begin{gathered} \mathrm{C} = \mathrm{C}_1 \text{ at } \mathrm{x} = 0 \text{ (for all t for transient drug transport)}, \\ \mathrm{C} = \mathrm{C}_2 \text{ at } \mathrm{x} = \mathrm{h} \text{ (for all t for transient drug transport)}, \\ \mathrm{C} = 0 \text{ for } 0 < \mathrm{x} < \mathrm{h} \ \ (\text{at } \mathrm{t} = 0 \text{ for transient drug transport}) \end{gathered} \tag{5}$$

Where $C_1$ is the constant drug concentration we give on the skin surface, $C_2$ is the drug concentration at the bottom of our skin model, x is the distance between skin surface and a specific point in the skin, h is the thickness of the skin. For transient simulations, $C_2$ is set to zero at the beginning and its cumulative values over time will be calculated using equation (4) until steady state is reached. In order to solve the differential equations (in 2D or 3D), additional boundary conditions should be applied to equations (1) and (4):

$$-\boldsymbol{n} \cdot \boldsymbol{N}_i = 0 \text{ at plane } \mathrm{y} = 0, \mathrm{l} \text{ and } \mathrm{z} = 0, \mathrm{w} \text{ (at all t for transient drug transport)} \tag{6}$$

Where $\mathbf{n}$ is the normal vector to the plane, $\mathbf{N}_i$ is the flux, y is the length between the front surface of the model and a specific point in the skin in longitudinal direction and the total length is l, z is

the width between the left surface of the model and a specific point in the skin in horizontal direction and the total width is w. The governing equations are implemented in commercial software COMSOL by importing the coordinates of the points on the skin surface and choosing the element sizes for different accuracy scales of FEM mesh. The parameters that are needed for the simulations can be either acquired from experimental data or using the theoretical values (e.g., correlations). If the transient model is applied which refers to equation (4), COMSOL can show the diffusion results at any time point before it reaches the steady state.

## 4. Results and discussion

### 4.1 Calculation of MN insertion depths based on histological images

Four histological images of MNs treated skin samples have been chosen for both 1100µm and 1400µm long MNs. The insertion depth of each image is then calculated using ImageJ software (Bethesda, MA, USA) [35] and the mean insertion depth of each group has been calculated. It is found that the average insertion depth of 1100µm and 1400µm long MNs are 0.53±0.054 mm and 0.7435±0.099 mm, respectively.

The theoretical insertion depth refers to the length of the MNs which are 1.1 mm and 1.4 mm, respectively. The full skin thickness is a constant value of 1.6mm, which is mentioned in the previous section.

The experimental data are obtained from our previous study effects of MNs on the permeability of insulin in skin [25]. Since a drug molecule that is larger than 500 Da cannot pass through the SC layer passively [36], we define that the diffusion coefficient for insulin (MW: 5808 Da) in the SC layer is negligible. The histological images also indicate that the MNs partially break the SC layer and mass transfer distance between the drug solution and the receptor compartment in a FDC is reduced. Therefore, the complex situation where the SC layer is involved will not be discussed in this paper and it is defined that the skin layer below the SC is the most relevant for modelling the drug delivery process. For this reason, we consider our skin model as one layer. Furthermore, we compare the passive diffusion in VE and diffusion in MN treated VEby using the diffusion coefficient of the viable epidermis. Based on these assumptions and data from our previous study, the diffusion coefficient ($D_{PD}$) is calculated as 1.3e-12 $m^2/s$ and the effective thickness of both MNs are deduced accordingly by applying equations (2) and (3), respectively. The insertion depths and skin thickness results acquired for insulin are shown in Fig. 13.

As shown in Fig. 13, we compare the full skin thickness with the calculated effective thickness of the skin, theoretical insertion depths (i.e., length of individual MN) and average MN insertion depths based on histological images. The results show that the effective thickness (and hence,

the mean path length for drug diffusion) is larger than the MN insertion depths based on the images but smaller than the MN lengths or real skin thickness.

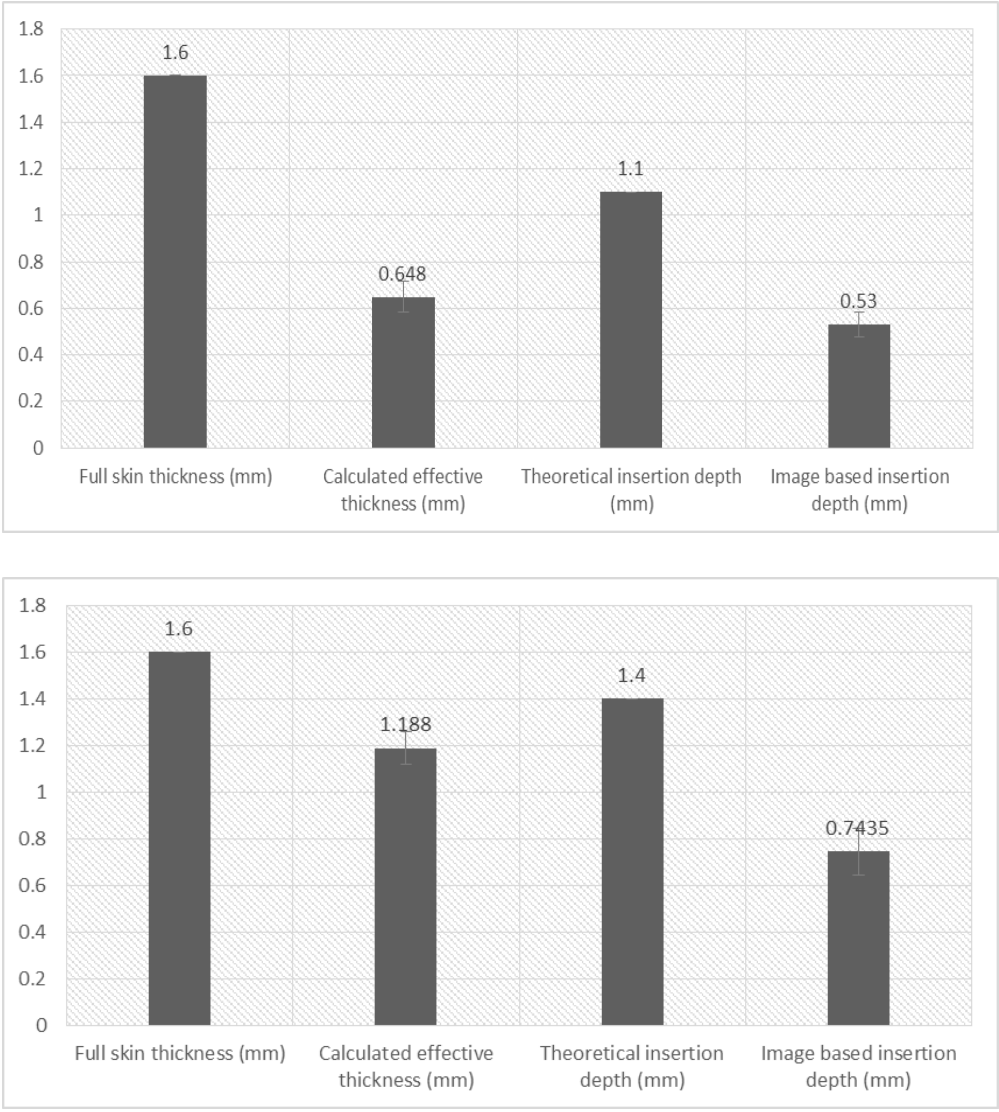


Fig. 13 Two sets of comparison: full skin thickness compared to the effective thickness after MNs insertion. The theoretical insertion relates to the insertion depth calculated from histological images. The effective thicknesses were calculated using data from insulin permeation study for 1100µm (top) and 1400µm (bottom) long MNs.

## 4.2 Numerical simulation of drug permeability/diffusion

### 4.2.1 Testing developed scheme for an ideal MN geometry

In order to test that the developed algorithm performs, we attempt to simulate an ideal geometry of MN (Fig. 14A) and define that the holes created by them in the skin match their size and shape. Therefore, the MN holes are well defined in terms of shapes and size (Fig. 14) and have no debris in the image, making them a good model to test that the developed scheme is working. As obvious, the modelling does not involve the use of a histological image in this case and the

simulation is done using the image of the MN geometry (0.5mm long) with some bends and complex features. We define that such a MN system has been applied according to a 'poke and patch' approach where the MNs have been applied on the skin, removed after creating the MN holes and a drug is then applied on the skin which penetrate into the holes. The drug molecule then diffuses into the skin through the viable epidermis. In effect, we simulate the drug permeation study in a typical Franz diffusion cell as discussed earlier [23].

The data for permeation of insulin from our previous experiment using Franz diffusion cells [25] have been chosen to carry out the numerical test. The drug concentration on the skin surface is set to a constant value of 1000ppm and the bottom surface of the skin is set as zero concentration which indicates a static system such as those seen in the receptor compartment in a Franz diffusion cell. The time duration insulin is defined to be 48 hr.

Fig. 14 and Fig. 15 show some of the results obtained for the case above. In Fig. 14 (C,D) we show the mesh used for the numerical simulation and concentrations distribution in the MN treated skin at steady state. Figure 15 shows the numerically calculated insulin concentration in the receptor compartment of a Franz diffusion cell with and without MN. The results indicate that insulin (molecular weight: 5808 Da) reaches 10% of its maximum concentration in the receptor compartment in FDC after 48 hr. It has also shown that MNs cause great effects on large size molecules because the trend lines between MNs enhanced diffusion and passive diffusion are distinct.

### 4.2.2. Numerical simulation of insulin permeation in a Franz diffusion cell

In this section, we will illustrate modelling using the image acquired from cryotome sliced skin sample captured by a microscope camera. The original and processed images are shown in Fig. 16. The simulation is then employed based on those 2D histological images. The MNs we applied are flat in structure with negligible thickness; therefore 2D images are sufficient for this study. However, the methodologies are general and therefore they can be applied for MN of any shapes and sizes provided their histological images are available.

The same initial and boundary conditions as discussed earlier are again applied for the purpose of this section. The numerical results for insulin concentration in the receptor compartment of a Franz diffusion cell are shown in Fig. 17. The insulin delivery has been shown higher amount of drug permeated and reduced lag time (time from initiation to the steady state). The simulated data from all the histological images are now averaged and compared with the experimental results of insulin from our previous study [25]. The initial concentration of the drugs and time durations of the simulation remain the same with the experiment condition. The results are

shown in Fig. 18. From the figure we can see that that the predicted concentration of insulin resembled well to the experimental results.

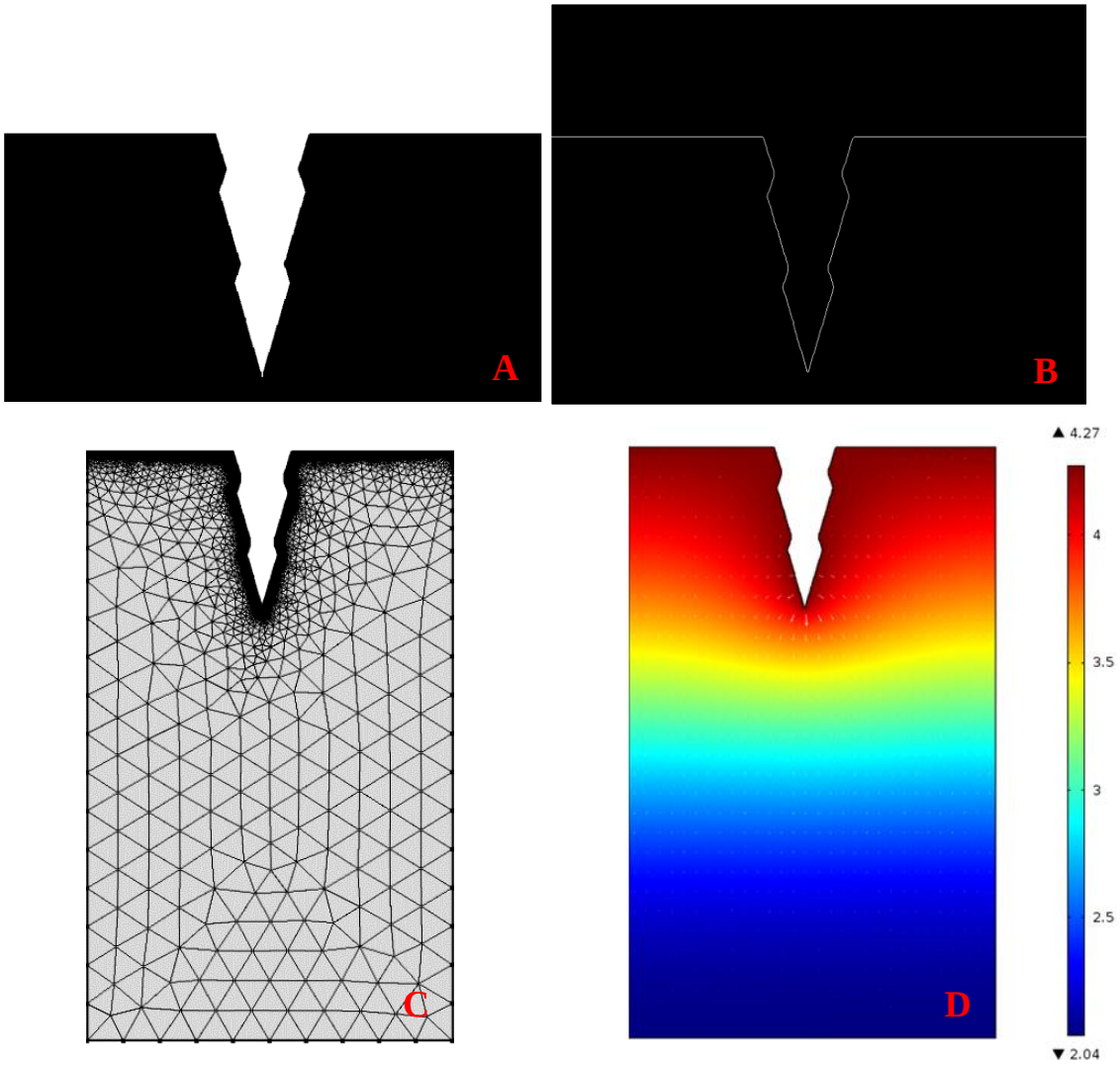


Fig.14 The process after the image is input into the program. A) The original image; B) The outline of the skin has been captured; C) The skin thickness has been adjusted to 1.6mm and the mesh using FEM has done; D) the simulation of the diffusion profile of the target drug molecule (insulin, in this study)

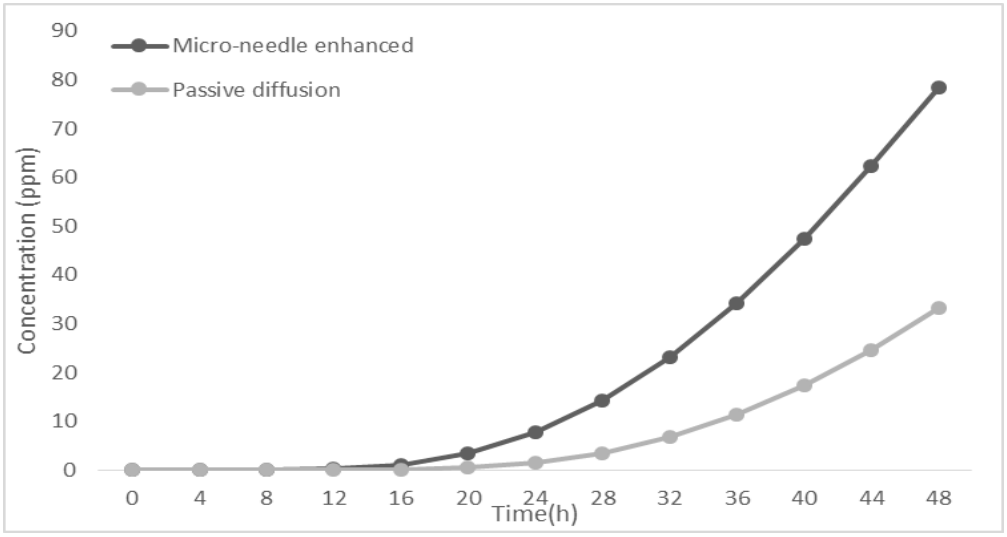


479

480 Fig.15 Insulin concentration profile of the passive diffusion and MNs enhanced diffusion based
481 on the ideal geometry in Fig 14. In both cases, only permeation in viable epidermis is considered.

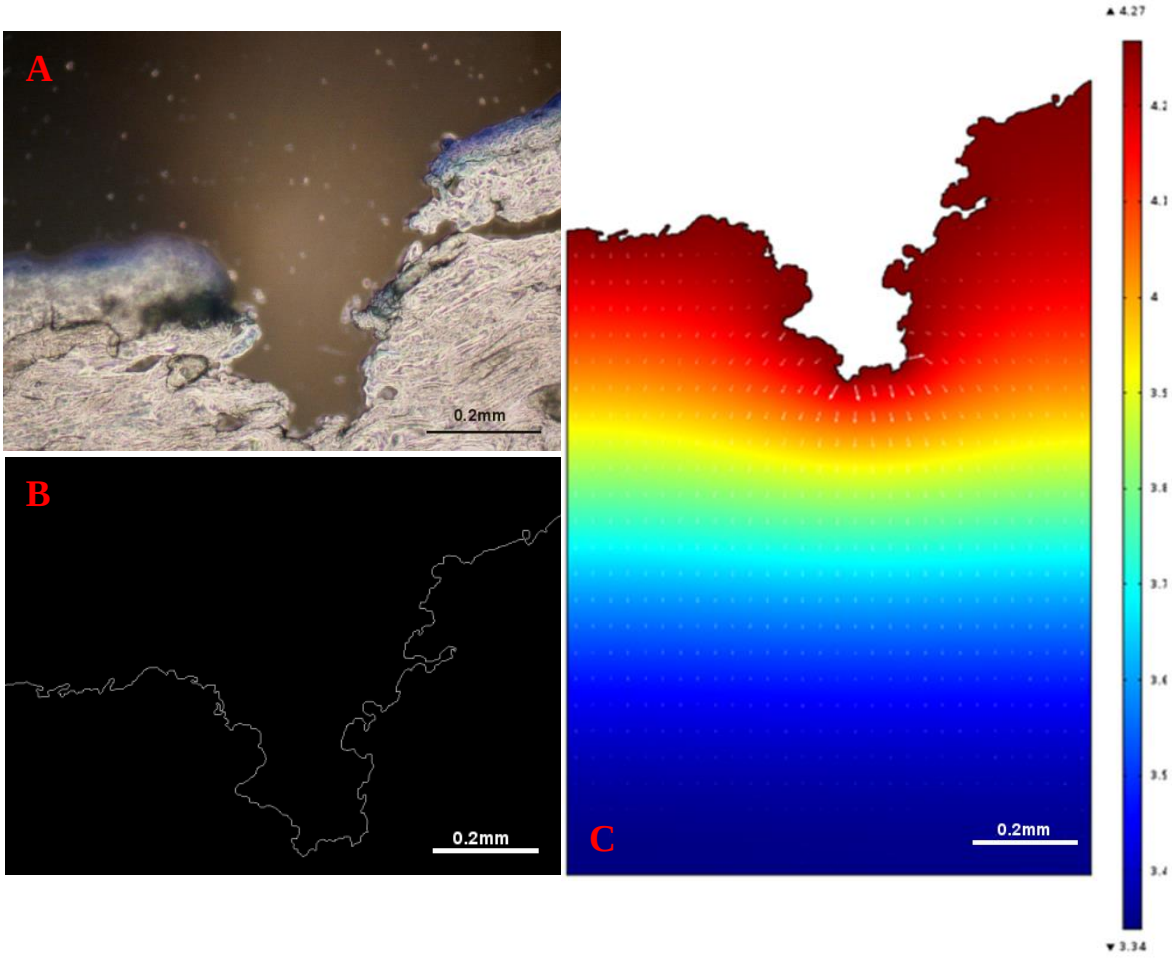


482

483 Fig. 16 The image from cryotome sliced skin is processed by program and simulated in
484 COMSOL. A) The original image; B) The outline of the skin has been captured; C) Simulated
485 diffusion profile of the target drug molecule (insulin, in this paper)

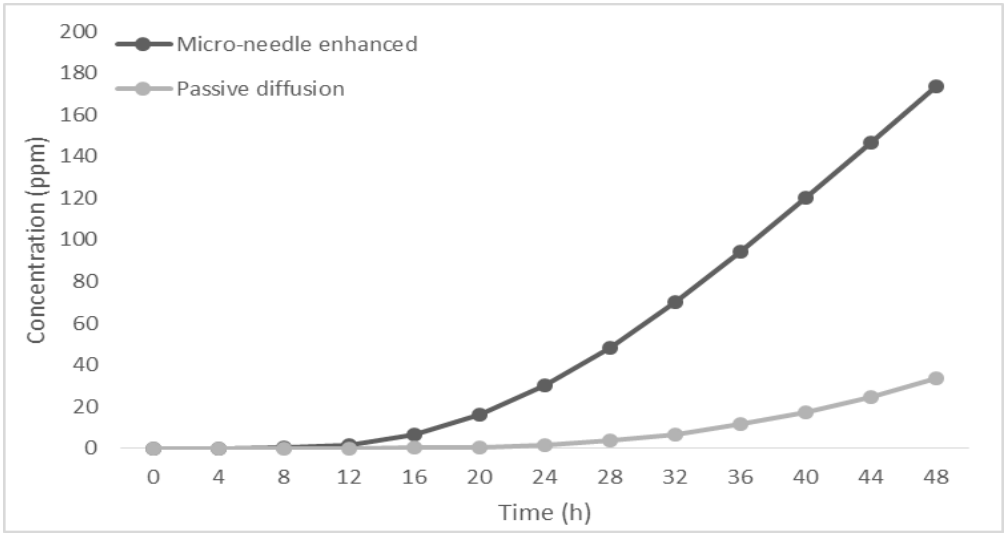


Fig. 17 The diffusion profile of the passive diffusion and MNs enhanced diffusion based on the imported model. Insulin concentrations in the receptor compartment of FDC have been calculated. In both cases, only permeation in viable epidermis is considered.

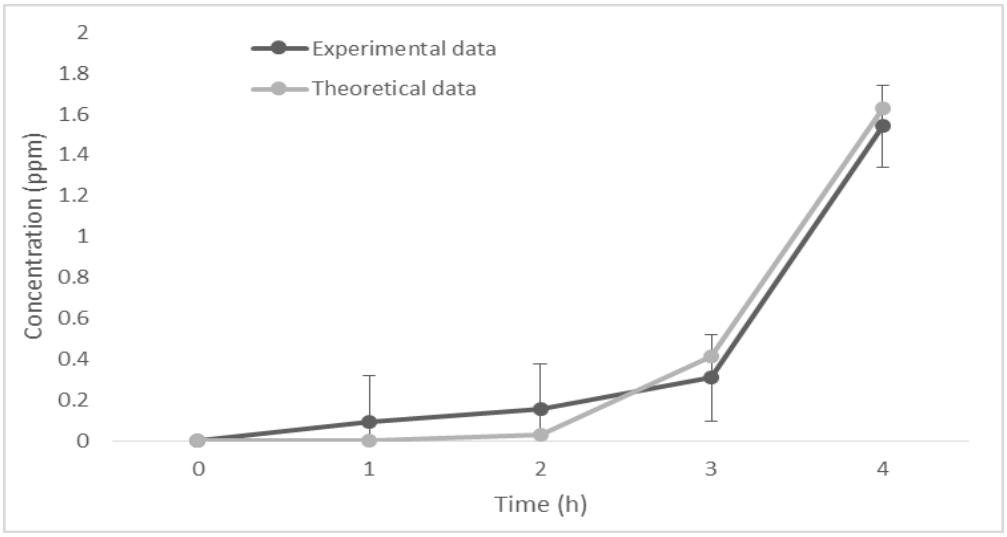


Fig. 18 Numerical simulation data compared to the experimental results from our previous papers [25]. The concentration profiles of insulin are presented.

### 4.2.3. Numerical simulation using images obtained from the literature

The third modelling scenario is based on a complex OCT image which we have collected from a published paper [37]. The OCT image has much lower resolution level than the images taken by the in-house camera in this study. Despite this, it is observed that the developed algorithm can depict the outline of the skin surface without losing significant details. The numerical modelling results using these images have been shown in Fig. 19. The image in this case shows that the MNs create lower insertion depth but more holes than previous images. Assuming that the MNs in this example are used to carry out an insulin permeation study, the same boundary conditions

are applied again on this image. The insulin concentrations in the receptor compartment of a FDC are shown in Fig. 20. The concentration profiles indicate that although the numbers of the holes increased as MNs are pierced into the skin, the diffusion rate is low compare to the passive diffusion. This also suggests that simply increasing the number of the MNs will not greatly increase the permeability in this case. The insertion depth and the geometry of the MNs may present higher impact to the diffusion rate.

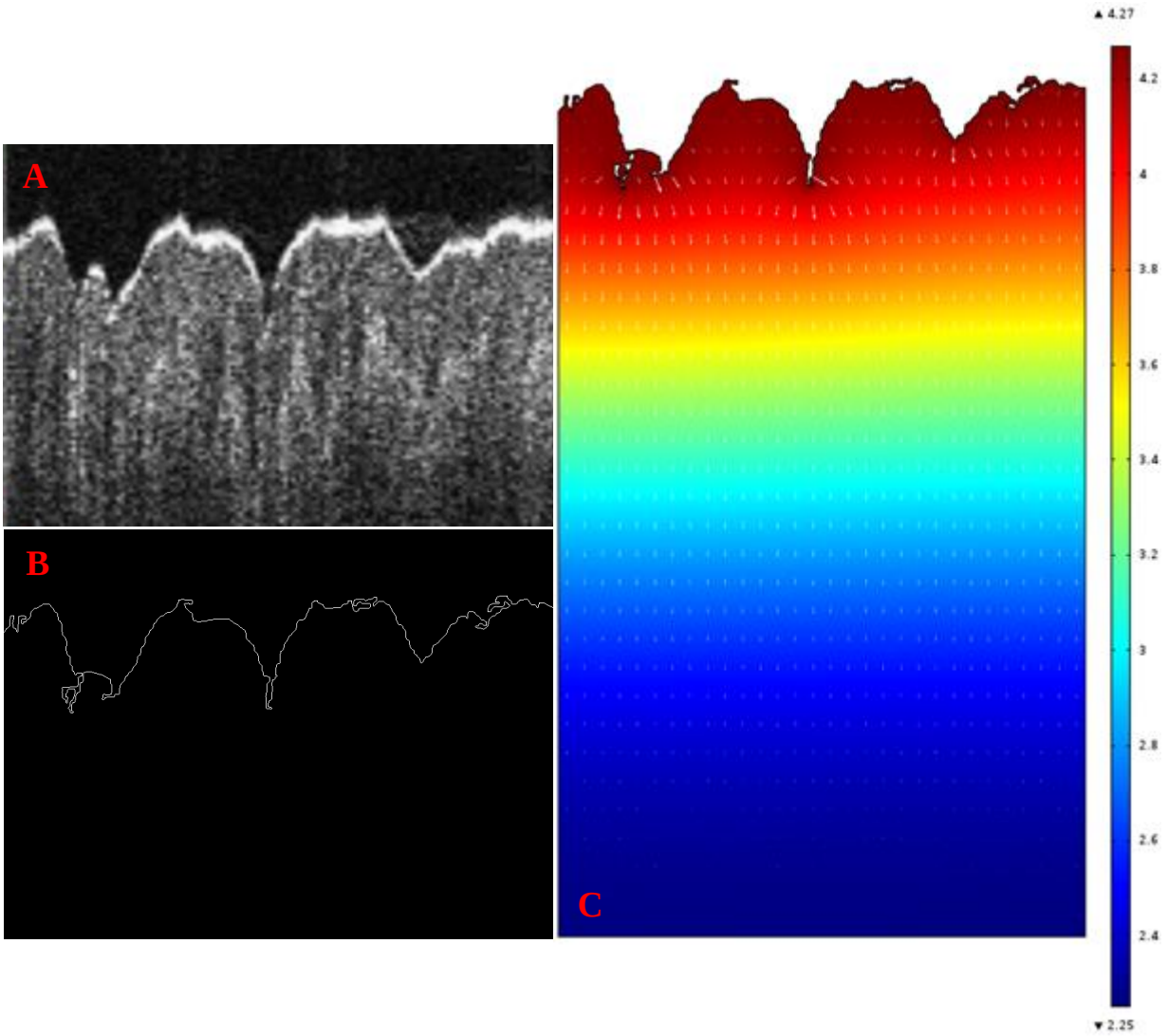


Fig.19 The OCT image is processed by the program and simulated in COMSOL. A) The original OCT image; B) The outline of the skin has been captured; C) the simulation of the diffusion profile of the target drug molecule [37].

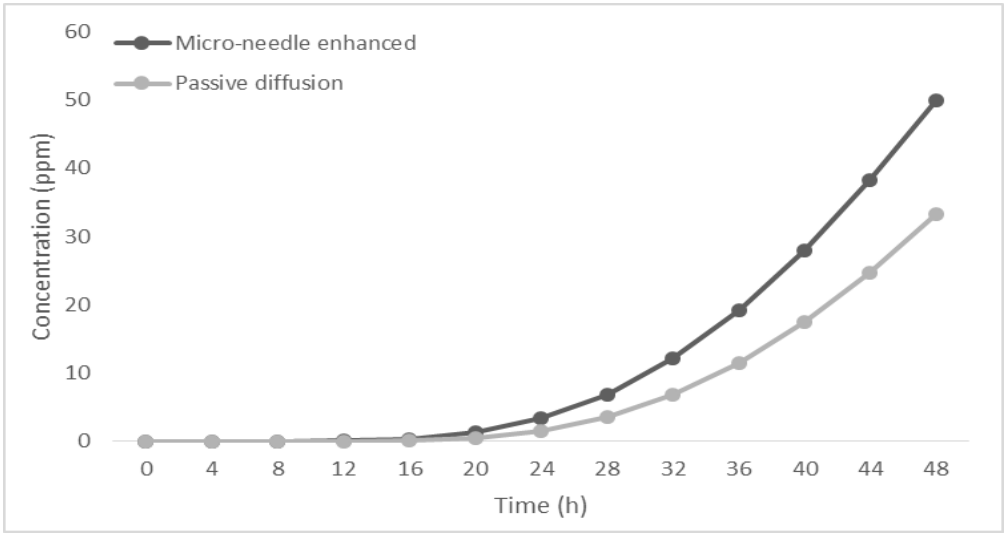


Fig. 20 The diffusion profile of the passive diffusion and MNs enhanced diffusion based on the model of Fig. 19. Insulin concentrations at receptor compartment of FDC have been calculated. In both cases, only permeation in viable epidermis is considered so as to have a meaningful comparison.

### 4.2.4. Numerical simulation of insulin permeation in 3D

The last case is an extension from the first scenario where we attempted to demonstrate simulation of 2D structured MNs. There are plenty of previous studies which have used 3D MNs model to simulate diffusion in TDD [38]. However, our 3D model is constructed from the pores created by MNs instead of building a model using the shape of MNs. Different slices of histological images from one MN cavity are combined to form a 3D model of the MN cavity and the accuracy of the reconstructed MN cavity will increase when more slices are involved. In this case, we choose the sample shape from Fig. 14 as the standard to maintain the consistency and illustrate the process by including another 8 slices to construct the 3D model. The profile of each sample slice is acquired using previous method and then all slices are imported to COMSOL as individual surfaces which are shown in Fig. 21. After all sample slices are imported into COMSOL, triangular and quadrilateral surface elements are created to connect one slice to its adjacent slices (Fig. 22A). These connected slices are then knitted into one complete solid computational domain and meshed using FEM, so the 3D boundary conditions from equation (5) and (6) can be applied accordingly (Fig. 22B). The same concentration (1000 ppm of insulin solution) is applied on the top surface of the model and the cumulative concentrations at the bottom surface are recorded for 48h with a 4h interval (Fig. 22C).

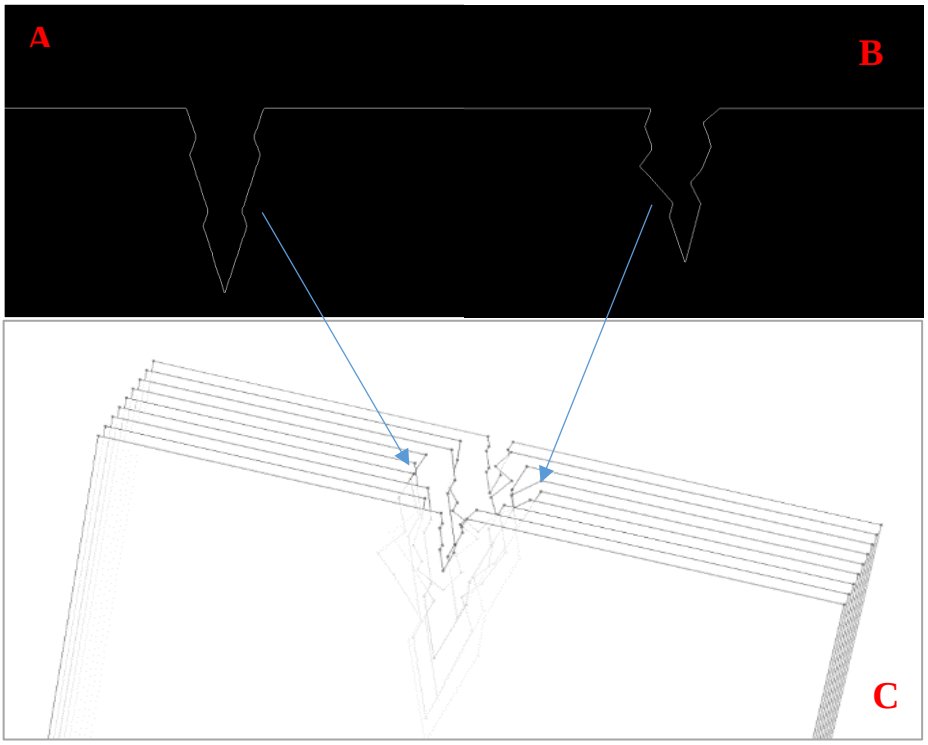


Fig. 21 The sample slices have been acquired individually and then imported into COMSOL. A) The profile of the sample slice from Fig. 14 which is located in the middle of all slices; B) Another sample slice located next to the standard; C) All 9 slices are imported into COMSOL for further study.

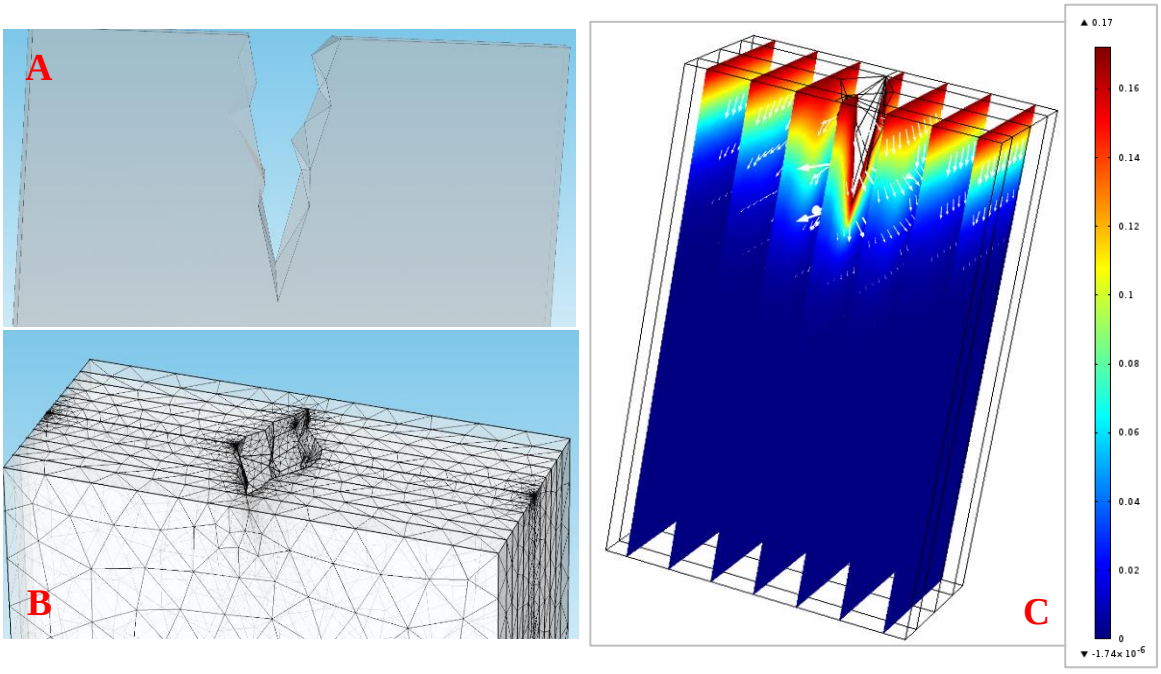


Fig. 22 The process of 3D modelling using sample image slices. A) Two adjacent slices are connected by surface elements; B) All slices are knitted to solid and meshed; C) The diffusion profile when insulin solution is mounted on the top surface of the model.

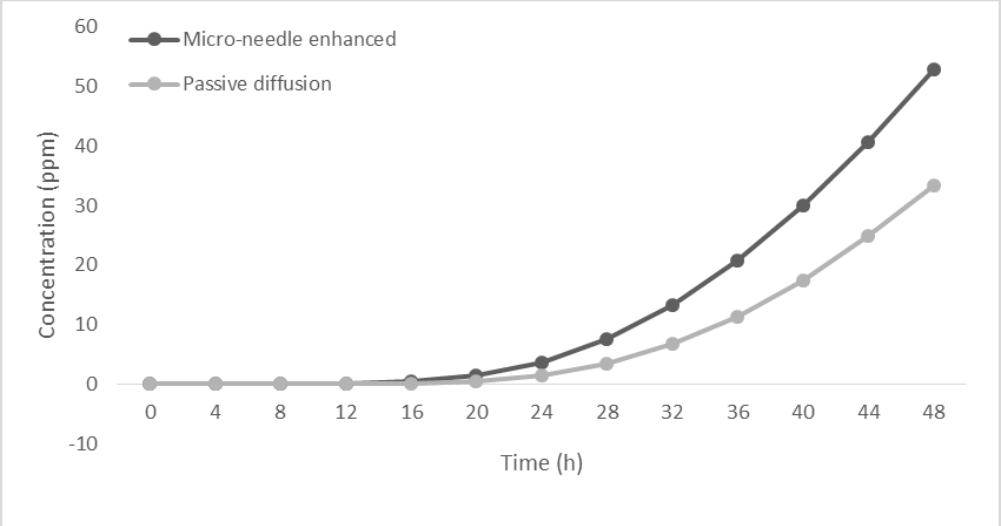


Fig. 23 The diffusion profile of the passive diffusion and MNs enhanced diffusion based on the model of Fig. 22. In both cases, only permeation in viable epidermis is considered

The numerical results for passive and MNs enhanced diffusion in VE are shown in Fig. 23. The cumulative concentrations of passive diffusion in the Fig. 22 are identical to the 2D results from Fig. 15 which indicates good consistency of the simulation. However, the concentrations of MNs enhanced diffusion of the 3D model are decreased due to the greater flux term in both horizontal and vertical directions. Based on this method, high quality 3D model of MNs treated skin can be achieved in the future if the acquired histological images are consistent and are of good quality. This paper aims to report on the development of the methodology and, therefore experimental results of 3D structured MNs will not be discussed.

## 5. Conclusion

Numerical simulation based on histological image using an new MATLAB program and COMSOL have been carried out which shows a great potential for accurate numerical modelling of MN enhanced drug delivery. The histological images provide the image of MNs created holes in the skin. This is hypothesised to be more accurate than simply assuming that the MN holes in the skin have the same shape and size as that of the of MNs' geometry. The histological images indicate an accurate depth of the hole which is required for the numerical simulation. The developed algorithm converts the real images to simulation required coordinates. After importing these data into a numerical simulator (e.g., COMSOL), the diffusion analysis can be easily carried out. It is expected that the developed paradigm for numerical simulation of MN based delivery would help the researches to design more efficient MNs systems.

566 **6. References**

567

[1] Teo AL, Shearwood C, Ng KC, Lu J, Moochhala S, "Transdermal microneedles for drug delivery applications," *Materials Science and Engineering,* no. 132, pp. 151-154, 2006.

[2] Li Y, Zhang PY, "Study on mechanical properties for modeling and simulation of microneedles for medical applications," *Applied Mechanics and Materials,* vol. 454, pp. 86-89, 2014.

[3] Kalluri H, Banga AK, "Microneedles and transdermal drug delivery," *Journal of Drug Delivery Science and Technology,* vol. 19, no. 5, pp. 303-310, 2009.

[4] Higuchi T, "Physical chemical analysis of percutaneous absorption process from creams and ointments," *Journal of the Society of Cosmetic Chemists,* vol. 11, no. 11, pp. 85-97, 1960.

[5] Al-Qallaf B, Das DB, "Optimizing microneedle arrays to increase skin permeability for transdermal drug delivery," *Annals of the New York Academy of Sciences,* no. 1161, pp. 83-94, 2009.

[6] Kalluri H, Banga AK, "Transdermal delivery of proteins," *AAPS PharmSciTech,* vol. 12, no. 1, pp. 431-441, 2011.

[7] Roxhed N, Gasser TC, Griss P, Holzapfel GA, Stemme G, "Penetration-enhanced ultrasharp microneedles and prediction on skin interaction for efficient transdermal drug delivery," *Journal of Microelectromechanical Systems,* vol. 16, no. 6, pp. 1429-1440, 2007.

[8] Brazzle J, Papautsky I, Frazier AB, "Micromachined needle arrays for drug delivery or fluid extraction: Design and fabrication aspects of fluid coupled arrays of hollow metallic microneedles," *IEEE Engineering in Medicine and Biology Magazine,* vol. 18, no. 6, pp. 53-58, 1999.

[9] Olatunji O, Das DB, Nassehi V, "Modelling transdermal drug delivery using microneedles: effect of geometry on drug transport behaviour," *Journal of Pharmaceutical Sciences,* vol. 101, no. 1, pp. 164-175, 2012.

[10] Windbergs M, Hansen S, Schroeter A, Schaefer UF, Lehr CM, Bouwstra J, "From the Structure of the Skin Barrier and Dermal Formulations to in vitro Transport Models for Skin Absorption Skin Research in the Netherlands and in Germany," *Skin Pharmacol Physiol.,* vol. 26, no. 4-6, pp. 317-330, 2013.

[11] Aggarwala P, Johnston CR, "Geometrical effects in mechanical characterizing of microneedle for biomedical applications," *Sensors and Actuators B,* vol. 102, no. 2, pp. 226-234, 2004.

[12] Al-Qallaf B, Das DB, "Optimization of square microneedle arrays for increasing drug permeability in skin," *Chemical Engineering Science,* vol. 63, no. 9, pp. 2523-2535, 2008.

[13] Al-Qallaf B, Das DB, "Optimizing microneedle arrays for transdermal drug delivery: extension to non-square distribution of microneedles," *Journal of Drug Targeting,* vol. 17, no. 2, pp. 108-122, 2009.

[14] Groves RB, Coulman SA, Birchall JC, Evans SL, "Quantifying the mechanical properties of human skin to optimise future microneedle device design," *Computer Methods in Biomechanics and Biomedical Engineering,* vol. 15, no. 1, pp. 73-82, 2012.

[15] Al-Qallaf B, Das DB, Mori D, Cui Z, "Modelling transdermal delivery of high molecular weight drugs from microneedle systems," *Philos Trans A Math Phys Eng Sci.,* vol. 365, no. 1861, pp. 2951-2967, 2007.

[16] Olatunji O, Das DB, Garland MJ, Belaid L, Donnelly RF, "Influence of array interspacing on the force required for successful microneedle skin penetration: theoretical and practical approaches," *J Pharm Sci.,* vol. 102, no. 4, pp. 1209-1221, 2013.

[17] Shuhu C, Nannan L, Jing C, "Finite element analysis of microneedle insertion into skin," *Micro & Nano Letters,* vol. 7, no. 12, pp. 1206-1209, 2012.

[18] Kalluri H, Kolli CS, Banga A, "Characterization of microchannels created by metal microneedles: Formation and closure," *AAPS Journal,* vol. 13, no. 3, pp. 473-481, 2011.

[19] Larrañeta E, Moore J, Vicente-Pérez EM, González-Vázquez P, Lutton R, Woolfson AD, Donnelly RF, "A proposed model membrane and test method for microneedle insertion studies," *International Journal of Pharmaceutics,* vol. 472, no. 1-2, pp. 65-73, 2014.

[20] Kim CS, Wilder SP, Ahn YC, Liaw LH, Chen Z, Kwon YJ, "Enhanced detection of early-stage oral cancer in vivo by optical coherence tomography using multimodal delivery of gold nanoparticles," *J Biomed Opt.,* vol. 14, no. 3, pp. 1-17, 2009.

[21] Cai B, Xia W, Bredenberg S, Engqvist H, "Self-setting bioceramic microscopic protrusions for transdermal drug delivery," *J Mater Chem B.,* vol. 2, no. 36, pp. 5992-5998, 2014.

[22] S. F. Littmarck S, "COMSOL Multiphysics(Version 4.4) [Computer program]," 1986. [Online]. Available: http://www.comsol.com/. [Accessed 2014 12 01].

[23] Han T, Das DB, "Permeability enhancement for transdermal delivery of large molecule using low-frequency sonophoresis combined with microneedles," *J.Pharm.Sci.,* vol. 102, no. 10, pp. 3614-3622, 2013.

[24] Nayak A, Babla H, Han T, Das DB, "Lidocaine carboxymethylcellulose with gelatine co-polymer hydrogel delivery by combined microneedle and ultrasound," *Drug Delivery,* pp. 1-12, 2014.

[25] Cheung K, Han T, Das DB, "Effect of Force of Microneedle Insertion on the Permeability of Insulin in Skin," *Journal of Diabetes Science and Technology,* vol. 8, no. 3, pp. 444-452, 2014.

[26] MathWorks, "Matlab (Version R2014a) [Computer program]," 1984. [Online]. Available: http://uk.mathworks.com/products/matlab/. [Accessed 16 11 2014].

[27] Canny J, "A Computational Approach To Edge Detection," *Pattern Analysis and Machine Intelligence,*

vol. 8, no. 6, pp. 679-698, 1986.

[28] Canny J, “Finding edges and lines in images,” Artificial Intelligence Lab Publications, Cambridge, MA, 1983.

[29] Svoboda T , Kybic J , Hlaváč V, Image Processing, Analysis & and Machine Vision - A MATLAB Companion, Boston, MA: Cengage Learning, 2007.

[30] Solomon C, Breckon T, Fundamentals of Digital Image Processing: A Practical Approach with Examples in Matlab, Hoboken, NJ: Wiley Blackwell, 2010.

[31] Baxes GA, Digital image processing: principles and applications, New York, NY: John Wiley & Sons, 1994.

[32] Davidson A, Al-Qallaf B, Das DB, “Transdermal drug delivery by coated microneedles: Geometry effects on effective skin thickness and drug permeability,” *Chemical Engineering Research and Design,* vol. 86, no. 11, pp. 1196-1206, 2008.

[33] Al-Qallaf B, Das DB, Davidson A, “Transdermal drug delivery by coated microneedles: geometry effects on drug concentration in blood,” *Asia-Pacific Journal of Chemical Engineering,* vol. 4, no. 6, pp. 845-857, 2009.

[34] Chaskalovic J, Finite Elements Methods for Engineering Sciences, Paris, France: Springer Verlag, 2008.

[35] Rasband W, “ImageJ (Version 1.48v) [Computer program],” 1997. [Online]. Available: http://rsb.info.nih.gov/ij/. [Accessed 16 11 2014].

[36] Brown MB, Martin GP, Jones SA, Akomeah FK, “Dermal and transdermal drug delivery systems: current and future prospects,” *Drug Delivery,* vol. 13, no. 3, pp. 175-187, 2006.

[37] Enfield J, O'Connell ML, Lawlor K, Jonathan E, O'Mahony C, Leahy M, “In-vivo dynamic characterization of microneedle skin penetration using optical coherence tomography,” *J Biomed Opt,* vol. 15, no. 4, pp. 1-7, 2010.

[38] Loizidou EZ, Williams NA, Barrow DA, Eaton MJ, McCrory J, Evans SL, Allender CJ, “Structural characterisation and transdermal delivery studies on sugar microneedles: Experimental and finite element modelling analyses,” *European Journal of Pharmaceutics and Biopharmaceutics,* vol. 89, pp. 224-231, 2014.

568

569